Mechanics of Materials 188 (2024) 104844

Contents lists available at ScienceDirect

Mechanics of Materials

journal homepage: www.elsevier.com/locate/mecmat

Editor invited article

A shear-lag model for laminated beams with extreme modulus mismatch between layers

Zheliang Wang [a], Hao Sheng [b], Xinyi Lin [b], Yifan Rao [a], Jia Liu [b], Nanshu Lu [a,*]

[a] Department of Aerospace Engineering and Engineering Mechanics, The University of Texas at Austin, TX, 78712, United States
[b] John A. Paulson School of Engineering and Applied Sciences, Harvard University, MA, 02134, United States

ARTICLE INFO

Keywords:
Flexible electronics
Shear-lag
Flexural rigidity
Multilayer beam
Elasticity

ABSTRACT

Multilayer laminated beams, comprised of alternating stiff and soft layers, are widely used in flexible electronics and photonics. These structures exhibit complex mechanical behaviors that deviate from the Euler–Bernoulli beam theory under conditions of extreme inter-layer modulus mismatch. Extending beyond prior studies on trilayer beams, we present an analytical framework for laminated beams with arbitrary number of layers subjected to various bending conditions, and validate our theory with finite element analysis. We define an equivalent flexural rigidity, exploring its dependence on position and deformation, and systematically examine the impact of the number of layers, applied deformation, layer properties, and the layer aspect ratio.

1. Introduction

The advent of flexible electronics has had a significant impact on a diverse range of applications, including flexible displays (Zhao et al., 2022), flexible sensors (Luo et al., 2023), wearable and implantable electronics (Sunwoo et al., 2021; Liu et al., 2022; Song et al., 2019), prosthetics (Chortos et al., 2016; Park et al., 2020), bio-mimetic electronic skins (Yang et al., 2019) and bionic eyes (Lee et al., 2018), and soft photonics (Geiger et al., 2020). A widely adopted structural design in flexible devices involves layering stiff functional layers with soft insulating or isolating layers. These functional layers can range from glass-based optical waveguides (Fig. 1a), copper interconnects in multilayer wearable electronics (Fig. 1b), to PZT films in a flexible energy harvester (Fig. 1c), and even flexible battery arrays (Fig. 1d). When there is a substantial mismatch in Young's modulus between the functional layers and the insulating or isolating layers, the mechanical behaviors of these laminated beams can significantly deviate from the Euler–Bernoulli beam theory due to the shear-lag effects.

The concept of 'shear-lag' was initially used to describe the nonuniform normal stress distribution observed in the flanges of box beams, which was found to 'lag' behind the predictions of the Euler–Bernoulli (E–B) theory due to the shear deformation of the unsupported flanges (Fig. 2(a)) (Reissner, 1938; Kuhn, 1939; Reissner, 1946). This understanding of shear-lag was soon extended to scenarios where the stress transfer via shear results in nonuniform normal stress distribution and lower stiffness, including tension panels, riveted tension members (Fig. 2(b)) (Fan, 1939; Williams, 1951), fibrous composite (Fig. 2(c)) (Cox, 1952), and nacre or nacre-inspired composites (Jackson et al., 1989; Ji and Gao, 2004; Jin et al., 2022). The shear-lag model for composites has been notably successful and has later been applied to laminated composites (Nairn and Mendels, 2001) and various nanocomposites (Weerasinghe et al., 2017; Gao and Li, 2005) (Fig. 2(d)). Most applications of shear-lag theories to composite materials are focused on the average tensile properties, with the notable exception of a recent work by Chen et al. (2023), where they studied the bending of nacre-like composites and proposed a bending deformable tension-shear model (BDTS) similar to this work but with the following differences. Firstly, the stiff layers in nacre-like structures are discontinuous, causing the results to depend on the length of platelets rather than the length of the whole beam. Moreover, the difference in the locations of breaks in different layers of the nacre-like structure also causes different boundary conditions from the laminated beams. Secondly, the methods they took were based on force equilibrium and assumed small deflection while our framework used an energy-based method and is applicable to large rotations. Finally, they only applied BDTS to the constant curvature case and resorted to the modified Timoshenko beam theory using the effective flexural rigidity for more complicated loading conditions, while our work present a general solution expressed in terms of applied bending curvature. Despite varying mathematical formulations, these shear-lag theories all feature a dimensionless parameter reflecting the characteristic aspect ratio and the modulus mismatch in a problem. As such, the shear-lag effect is more pronounced when the aspect ratio is small or when the modulus

Invited Editor: Yihui Zhang.

* Corresponding author.
E-mail address: nanshulu@utexas.edu (N. Lu).

https://doi.org/10.1016/j.mechmat.2023.104844
Received 21 August 2023; Received in revised form 14 October 2023; Accepted 21 October 2023
Available online 31 October 2023
0167-6636/© 2023 Elsevier Ltd. All rights reserved.

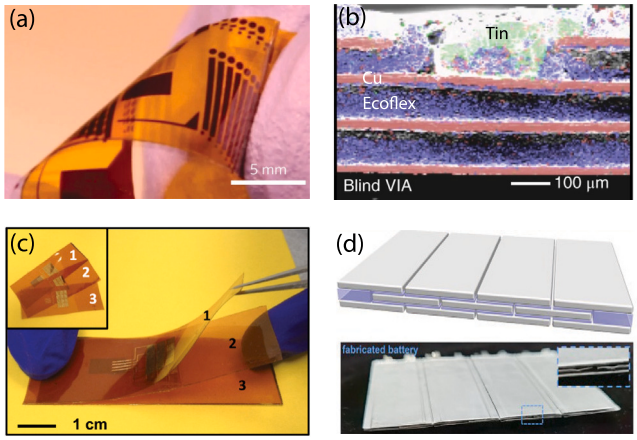


Fig. 1. Examples of flexible devices in the form of laminated beams with extreme modulus mismatch. (a) Chalcogenide glass-based flexible photonics (Li et al., 2014). (b) Multilayer stretchable heater (Huang et al., 2018). (c) Multilayer flexible energy harvester (Su et al., 2015). (d) Flexible battery (Li et al., 2022).

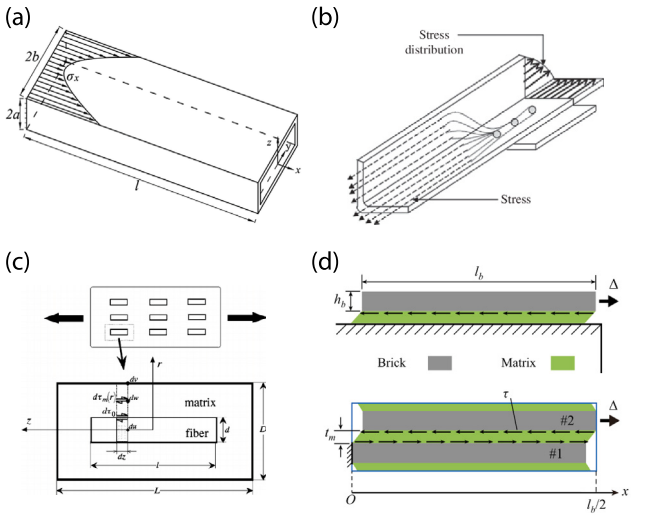


Fig. 2. Existing shear-lag examples: (a) Nonuniform normal stress distribution in the flange of box beams (Singh et al., 2020), (b) nonuniform normal stress distribution near the junction of a tension member (Priya et al., 2013), (c) reduced modulus in a fibrous composite due to shear deformation in the matrix (Murasawa et al., 2005), (d) two schematics of shear-lag model used for laminated nanocomposites (He et al., 2022).

mismatch is large. These models also predict a spatially nonuniform stress distribution, represented in the form of hyperbolic functions.

While not explicitly referred to as shear-lag, the reduced bending stiffness observed in multilayer 2D materials bears a conceptual resemblance to the laminated beams investigated in this work, where the weak tangential interlayer interactions are similar to the shear deformability of the soft layers in laminated beams (Shen and Wu, 2012; Chen et al., 2015; Liu et al., 2013). Huang et al. (2023) developed an analytical framework for multilayer 2D materials under arbitrary loading and applied the framework to the bending stiffness under three-point bending. They also constructed a deformation-mode phase diagram based on two universal characteristic lengths. The problem of 2D materials differs from the laminated beams in that the layer and interlayer properties are constant from layer to layer, while the laminated beams for flexible electronics may involve different materials and dimensions for each layer. Moreover, they did not provide explicit results on membrane strains, which is important for flexible electronics. Recent studies also incorporated interlayer slip through a periodic interfacial potential energy, which introduces non-linearity to the problem and results in a unique size dependence that is distinct from conventional shear-lag problems (Huang, 2020; Ma et al., 2021).

Li et al. (2014) pioneered in exploring the unconventional mechanical behaviors of laminated beam with extreme modulus mismatch. They discovered that a flexible photonic device with an SU8-silicone-polyimide laminate exhibits two mechanical neutral axes, contradicting the kinematic assumption used in the E–B beam theory that planar cross-sections remain planar. This phenomena and related theory has been since known as the 'split of neutral axis'. This discovery was later confirmed by Lee et al. (2019) using digital image correlation for full field deformation measurement of multilayer laminated beams. Li et al. (2014) proposed an analytical modeling of the phenomena by employing force balance and fitting one parameter to the FEA results. Shi et al. (2014) employed an energy-based analytical framework that eliminated the need for any fitting parameters. Su et al. (2015) were the first to propose that the soft layers within the multilayer laminated beam act as shear lags, and included the shear energy of the soft layer in their analysis. The analytical framework, which showed excellent agreement with FEA results for a trilayer beam conforming to a cylindrical surface, has been successfully applied to other deformation modes and device configurations (Li et al., 2017, 2022, 2016).

Prior work in this field has primarily concentrated on specific deformation types and fixed number of layers, with focuses on strain distribution analysis to prevent failure during bending. However, the importance of evaluating the structural stiffness of laminated beams is manifested by the growing significance of soft implantable bioelectronics such as neuroprobes (Sunwoo et al., 2021; Lecomte et al., 2018) and the electronic dura mater (Minev et al., 2015), where minimizing bending stiffness is key to reducing immune responses. This study broadens the framework outlined by Li et al. (2016) to encompass laminated beams with arbitrary number of layers under any bending condition. The rest of paper is organized as follows. Section 2 details the proposed theoretical framework and the FEA used to validate the analytical solution. Section 3 presents the results on multilayer beam conforming to a rounded wedge, defines an equivalent flexural rigidity, and explores the effects of various parameters. Section 4 probes the theoretical upper and lower bounds of flexural rigidity in relation to applied deformation, dimensionless control parameter, and layer number. Finally, Section 5 concludes our work.

2. Method

2.1. Analytical model

Fig. 3(a) illustrates the initial configuration of a straight laminated beam consisting of 2N + 1 layers with a length of L. The ith layer has height h_i, Young's modulus E_i and Poisson's ratio ν_i. The odd-numbered layers are much stiffer than the even-numbered layers. We develop an analytical framework for the laminated beam subject to various bending conditions described by an imposed bending curvature $\kappa(x)$ along the bottom of the beam (Fig. 3(b)). In this framework, each stiff layer is assumed to obey the kinematic assumption that cross section remain planar and perpendicular to the longitudinal axis; The stretching energy and bending energy are neglected due to the small modulus of the soft layers and we assume the shear to be the dominant mechanical deformation in the soft layers. As a demonstration, the results are applied to the cases where the beam conforms to a rounded wedge (Fig. 3(c)) and two arcs in the opposite sides of the beam (Fig. 3(d)).

Let $\mathbf{u} = \left(u_1, u_3, \ldots, u_{2N+1}\right)^T$ be the vector of axial displacement, where u_{2k-1} is the axial displacement at the central axis of the stiff layers. The membrane strains in the stiff layers are written as:

$$\boldsymbol{\epsilon} = \left(\epsilon_1, \epsilon_3, \ldots, \epsilon_{2N+1}\right)^T = \frac{\mathbf{du}}{\mathrm{d}x}. \tag{1}$$

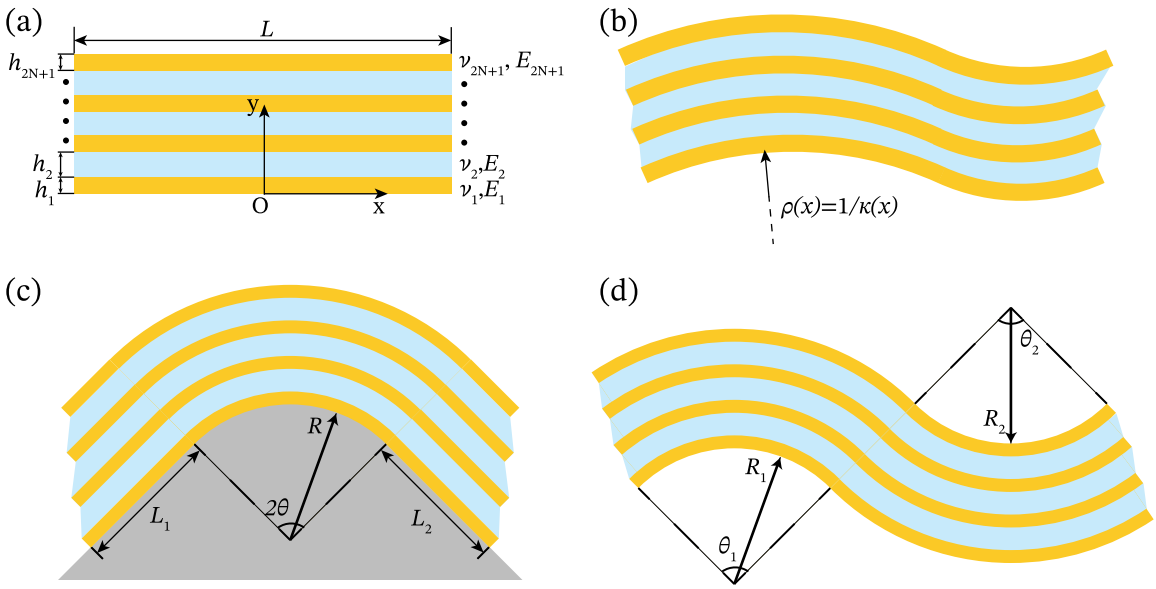


Fig. 3. Schematics of a multilayer laminated beam with extreme modulus mismatch. Golden color represents stiff layers and light blue represents soft layers. (a) The undeformed, stress-free configuration. (b) The deformed configuration with arbitrary bending curvatures. (c) The deformed configuration on a rounded wedge. (d) The deformed configuration on two cylinders. (For interpretation of the references to color in this figure legend, the reader is referred to the web version of this article.)

In this work, the laminated beams are assumed to be slender. The thickness change is neglected due to the minimal transverse stress caused by the deformation considered in this work. As a result, the deformed layers remain parallel in the deformed configuration, and the curvature at the center of ith layer can be written as:

$$\kappa_i = \frac{1}{\rho_i} = \frac{1}{y_i + 1/\kappa} = \frac{\kappa}{1+\kappa y_i}, \tag{2}$$

where y_i is the y coordinate of the center of the ith layer.

As shown in Fig. 4, the shear strain γ_{2k} in the soft layer $2k$ can be expressed geometrically as:

$$\begin{aligned}\gamma_{2k} &\approx \frac{\angle FEC + \angle ECD}{2} \approx \frac{\widehat{\mathrm{ED}} + \widehat{\mathrm{FC}}}{2\overline{AB}} \\ &= \frac{\widehat{\mathrm{BD}} - \widehat{\mathrm{BE}} + \widehat{\mathrm{AC}} - \widehat{\mathrm{AF}}}{2\overline{AB}}.\end{aligned} \tag{3}$$

Utilizing the kinematic assumptions in the stiff layers, $\widehat{\mathrm{BD}}$, $\widehat{\mathrm{BE}}$, $\widehat{\mathrm{AC}}$, and $\widehat{\mathrm{AF}}$ can be related to the deformation of the adjacent layers as:

$$\begin{aligned}\widehat{\mathrm{BD}} &= \frac{\int_0^x \left(y_{2k} + h_{2k}/2 + 1/\kappa\right) ds}{\int_0^x \left(y_{2k-1} + 1/\kappa\right) ds} \left(x + u_{2k-1}\right), \\ \widehat{\mathrm{AC}} &= \frac{\int_0^x \left(y_{2k} - h_{2k}/2 + 1/\kappa\right) ds}{\int_0^x \left(y_{2k-1} + 1/\kappa\right) ds} \left(x + u_{2k-1}\right), \\ \widehat{\mathrm{BE}} &= \frac{\int_0^x \left(y_{2k} + h_{2k}/2 + 1/\kappa\right) ds}{\int_0^x \left(y_{2k+1} + 1/\kappa\right) ds} \left(x + u_{2k+1}\right), \\ \widehat{\mathrm{AF}} &= \frac{\int_0^x \left(y_{2k} - h_{2k}/2 + 1/\kappa\right) ds}{\int_0^x \left(y_{2k+1} + 1/\kappa\right) ds} \left(x + u_{2k+1}\right).\end{aligned} \tag{4}$$

Substituting Eq. (4) into Eq. (3), we have:

$$\begin{aligned}\gamma_{2k} &= \frac{1}{h_{2k}} \left[r^{2k}_{2k-1}(x+u_{2k-1}) - r^{2k}_{2k+1}(x+u_{2k+1})\right], \\ r^j_j &= \frac{f_i}{f_j}, \quad f_i = 1 - y_i \frac{K(x)}{x}, \quad K(x) = \int_0^x \kappa(s) ds.\end{aligned} \tag{5}$$

Following Li et al. (2016), the total energy is the sum of the bending and stretching energy in the stiff layers and the shear energy in the soft layers:

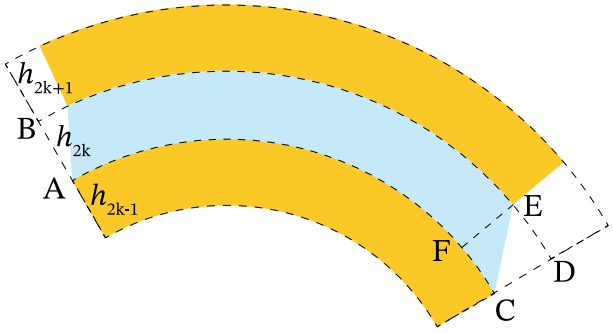


Fig. 4. Schematic illustration for calculating the shear strain in the soft layers from the curvature and axial displacement in the adjacent stiff layers.

$$\begin{aligned}U &= U^{stretch} + U^{bend} + U^{shear}, \\ U^{stretch} &= \sum_{k=1}^{k=N+1} \int_{-L}^{L} \frac{1}{2} \overline{EA}_{2k-1} \epsilon^2_{2k-1} dx, \\ U^{bend} &= \sum_{k=1}^{k=N+1} \int_{-L}^{L} \frac{1}{2} \overline{EI}_{2k-1} \kappa^2_{2k-1} dx, \\ U^{shear} &= \sum_{k=1}^{k=N} \int_{-L}^{L} \frac{1}{2} G_{2k} h_{2k} \gamma^2_{2k} dx.\end{aligned} \tag{6}$$

where $\overline{EA}_i = E_i h_i / \left(1-\nu_i^2\right)$ is the axial modulus of the ith layer, $\overline{EI}_i = E_i h_i^3 / \left[12(1-\nu_i^2)\right]$ is the flexural rigidity of the ith layer, and $G_i = \frac{E_i}{2(1+\nu_i)}$ is the shear modulus of ith layer.

The governing equation and the boundary condition can be obtained by substituting Eqs. (1), (2), (3) into Eq. (6) and taking the variation $\delta U = 0$:

$$\mathbf{K} \frac{\mathrm{d}^2 \mathbf{u}}{\mathrm{d}x^2} = \mathbf{A}\mathbf{u} - \mathbf{b}, \tag{7}$$

$$\left.\frac{\mathrm{d}\mathbf{u}}{\mathrm{d}x}\right|_{x=-L} = \left.\frac{\mathrm{d}\mathbf{u}}{\mathrm{d}x}\right|_{x=L} = 0, \tag{8}$$

where

$$\mathbf{K}=\begin{bmatrix}\overline{EA}_1 & & & & \\ & \overline{EA}_3 & & & \\ & & \overline{EA}_5 & & \\ & & & \ddots & \\ & & & & \overline{EA}_{2N+1}\end{bmatrix},$$

$$\mathbf{A}=\begin{bmatrix}B_{11}^1 & B_{12}^1 & & & & \\ B_{12}^1 & B_{22}^1+B_{11}^2 & B_{12}^2 & & & \\ & B_{12}^2 & B_{22}^2+B_{11}^3 & \ddots & & \\ & & \ddots & \ddots & B_{12}^N & \\ & & & B_{12}^N & B_{22}^N\end{bmatrix},$$

$B_{11}^k=\frac{G_{2k}}{h_{2k}}r_{2k-1}^{2k}r_{2k-1}^{2k}$, $B_{12}^k=\frac{G_{2k}}{h_{2k}}r_{2k-1}^{2k}r_{2k+1}^{2k}$, and $B_{22}^k=\frac{G_{2k}}{h_{2k}}r_{2k+1}^{2k}r_{2k+1}^{2k}$, and

$$\mathbf{b}=\begin{bmatrix}\frac{G_2}{h_2}r_1^2\left(-r_1^2+r_3^2\right)\\ \frac{G_4}{h_4}r_3^4\left(-r_3^4+r_5^4\right)+\frac{G_2}{h_2}r_3^2\left(-r_3^2+r_1^2\right)\\ \frac{G_6}{h_6}r_5^6\left(-r_5^6+r_7^6\right)+\frac{G_4}{h_4}r_5^4\left(-r_5^4+r_3^4\right)\\ \vdots\\ \frac{G_{2N}}{h_{2N}}r_{2N+1}^{2N}\left(-r_{2N+1}^{2N}+r_{2N-1}^{2N}\right)\end{bmatrix}x.$$

Here **K** is the matrix representing the axial rigidity of the stiff layers. **A** represents the interaction of stiff layers through the shear-lag effect of the sandwiched soft layers. **b** is a vector representing the applied bending.

When N = 1 and $\kappa(x)=1/R$, the governing equation Eq. (7) reduces to the equations previously reported by Li et al. (2016). To derive an analytical solution to Eq. (7) in terms of applied bending curvature κ, linearization and nondimensionalization are implemented. It is assumed that the radius of curvature is much larger than the total thickness of the beam, i.e. $\kappa h_i < \kappa\sum h_i \ll 1$. The governing equation and the boundary condition reduce to:

$$\frac{\mathrm{d}^2\mathbf{u}}{\mathrm{d}\hat{x}^2}=\Pi^2\left[\hat{\mathbf{C}}\hat{\mathbf{A}}\mathbf{u}-\hat{\mathbf{C}}\hat{\mathbf{b}}(h_1+h_2)\int_0^{\hat{x}}\kappa(s)ds\right], \tag{9}$$

$$\left.\frac{\mathrm{d}\mathbf{u}}{\mathrm{d}\hat{x}}\right|_{\hat{x}=-1}=\left.\frac{\mathrm{d}\mathbf{u}}{\mathrm{d}\hat{x}}\right|_{\hat{x}=-1}=0, \tag{10}$$

where $\hat{x}=x/L$ is the normalized coordinate, $\Pi=\sqrt{\left(1-\nu_1^2\right)\frac{L^2}{h_1h_2}\frac{G_2}{E_1}}$ is the dimensionless shear-lag number reflecting the interplay between modulus mismatch and the layer aspect ratio,

$$\hat{\mathbf{C}}=\begin{bmatrix}1 & & & & \\ & \frac{\overline{EA}_1}{\overline{EA}_3} & & & \\ & & \frac{\overline{EA}_1}{\overline{EA}_5} & & \\ & & & \ddots & \\ & & & & \frac{\overline{EA}_1}{\overline{EA}_{2N+1}}\end{bmatrix},$$

$$\hat{\mathbf{A}}=\begin{bmatrix}1 & -1 & & & & \\ -1 & 1+\frac{G_4}{h_4}\frac{h_2}{G_2} & -\frac{G_4}{h_4}\frac{h_2}{G_2} & & & \\ & -\frac{G_4}{h_4}\frac{h_2}{G_2} & \ddots & \ddots & & \\ & & \ddots & \ddots & -\frac{G_{2N}}{h_{2N}}\frac{h_2}{G_2} & \\ & & & -\frac{G_{2N}}{h_{2N}}\frac{h_2}{G_2} & \frac{G_{2N}}{h_{2N}}\frac{h_2}{G_2}\end{bmatrix},$$

$$\hat{\mathbf{b}}=\begin{bmatrix}\frac{0.5h_1+0.5h_3+h_2}{h_1+h_2}\\ \frac{G_4}{h_4}\frac{h_2}{G_2}\frac{0.5h_3+0.5h_5+h_4}{h_1+h_2}-\frac{0.5h_1+0.5h_3+h_2}{h_1+h_2}\\ \frac{G_6}{h_6}\frac{h_2}{G_2}\frac{0.5h_5+0.5h_7+h_6}{h_1+h_2}-\frac{G_4}{h_4}\frac{h_2}{G_2}\frac{0.5h_3+0.5h_5+h_4}{h_1+h_2}\\ \vdots\\ -\frac{G_{2N}}{h_{2N}}\frac{h_2}{G_2}\frac{0.5h_{2N-1}+0.5h_{2N+1}+h_{2N}}{h_1+h_2}\end{bmatrix}.$$

The general solution to Eq. (9) is:

$$\begin{aligned}\mathbf{u}=\sum_{i=2}^{N+1}&\left[\left(C_i+\int_0^{\hat{x}}\kappa(s)\sinh(\Pi\hat{\lambda}_i s)ds\right)\sinh\left(\Pi\hat{\lambda}_i\hat{x}\right)\right.\\&+\left(D_i-\int_0^{\hat{x}}\kappa(s)\cosh(\Pi\hat{\lambda}_i s)ds\right)\cosh\left(\Pi\hat{\lambda}_i\hat{x}\right)\\&\left.+\int_0^{\hat{x}}\kappa(s)ds\right]\frac{(h_1+h_2)g_i}{\hat{\lambda}_i^2}\hat{\mathbf{v}}_i+\left[C_1+D_1\hat{x}\right]\hat{v}_1.\end{aligned} \tag{11}$$

where $\hat{\lambda}_i^2$ is the eigenvalue of $\hat{\mathbf{C}}\hat{\mathbf{A}}$ in ascending orders, $\hat{\mathbf{v}}_i$ is the corresponding unit eigenvector, and $\hat{\mathbf{C}}\hat{\mathbf{b}}=\sum_{i=1}^{i=N+1}g_i\mathbf{v}_i$. It can be shown that $\lambda_1=g_1=0$, $\lambda_i^2>0$, and that and all eigenvectors are real (Appendix A). In general, the eigenvalue $\hat{\lambda}_i$ and eigenvector $\hat{\mathbf{v}}_i$ cannot be written out in an explicit analytical expression. In this work, we calculate $\hat{\lambda}_i$ and $\hat{\mathbf{v}}_i$ numerically using the built-in function 'eig' in Matlab.

The constants $C_1, D_1, C_2, D_2, \ldots, C_{N+1}, D_{N+1}$ are determined by substituting boundary condition Eq. (8) into Eq. (11):

$$\begin{cases}C_1=D_1=0\\ C_i=\int_0^1\kappa^{\mathrm{S}}(s)\dfrac{\sinh\left(\Pi\hat{\lambda}_i(1-s)\right)}{\cosh\left(\Pi\hat{\lambda}_i\right)}ds\\ D_i=\int_0^1\kappa^{\mathrm{A}}(s)\dfrac{\sinh\left(\Pi\hat{\lambda}_i(1-s)\right)}{\sinh\left(\Pi\hat{\lambda}_i\right)}ds\end{cases} \tag{12}$$

where $\kappa^{\mathrm{S}}(s)=\frac{1}{2}(\kappa(s)+\kappa(-s))$ and $\kappa^{\mathrm{A}}(s)=\frac{1}{2}(\kappa(s)-\kappa(-s))$ are the symmetric part and asymmetric part of the function κ respectively.

In practical applications, the membrane strains in the stiff layers are of particular interest to avoid the device failure. The membrane strains are derived by taking derivatives of the displacement as:

$$\begin{aligned}\epsilon=\sum_{i=2}^{N+1}&\left[\left(C_i+\int_0^{\hat{x}}\kappa(s)\sinh(\Pi\hat{\lambda}_i s)ds\right)\cosh\left(\Pi\hat{\lambda}_i\hat{x}\right)\right.\\&\left.+\left(D_i-\int_0^{\hat{x}}\kappa(s)\cosh(\Pi\hat{\lambda}_i s)ds\right)\sinh\left(\Pi\hat{\lambda}_i\hat{x}\right)\right]\\&\frac{\Pi(h_1+h_2)g_i}{\hat{\lambda}_i}\hat{\mathbf{v}}_i.\end{aligned} \tag{13}$$

2.1.1. Case I: conforming to rounded wedge

Now we consider a special case where the beam is conformed to a rounded wedge (Fig. 3c) with radius R and angle θ. The curvature of the deformed shape is:

$$\kappa=\begin{cases}1/R & 0\le|\hat{x}|\le\frac{R\theta}{L}\\ 0 & \frac{R\theta}{L}\le|\hat{x}|\le1\end{cases} \tag{14}$$

For simplification, we focus on the case where $E_1=E_3=\cdots=E_{2N+1}=E_h$, $\nu_1=\nu_3=\cdots=\nu_{2N+1}=\nu_h$, $h_1=h_3=\cdots=h_{2N+1}=h_h$, $G_2=G_4=\cdots=G_{2N}=G_s$, $h_2=h_4=\cdots=h_{2N}=h_s$. In this case, $\hat{\mathbf{C}}\hat{\mathbf{A}}$ reduces to a symmetric matrix and we have:

$$g_i=\hat{\mathbf{b}}\cdot\hat{\mathbf{v}}_i. \tag{15}$$

Plugging Eqs. (12), (14), and (15) into Eq. (11), we have:

$$\mathbf{u}=\frac{h_1+h_2}{R}\sum_{i=2}^{N+1}f_i(x)\frac{\hat{\mathbf{b}}\cdot\hat{\mathbf{v}}_i}{\hat{\lambda}_i^2}\hat{\mathbf{v}}_i. \tag{16}$$

$$f_i(\hat{x})=\begin{cases}x-\dfrac{\cosh\left(\Pi\hat{\lambda}_i\frac{L_1}{L}\right)\sinh\left(\Pi\hat{\lambda}_i\hat{x}\right)}{\Pi\hat{\lambda}_i\cosh\left(\Pi\hat{\lambda}_i\right)} & |\hat{x}|<\frac{R\theta}{L}\\ R\theta-\dfrac{\sinh\left(\Pi\hat{\lambda}_i\frac{R\theta}{L}\right)\cosh\left(\Pi\hat{\lambda}_i(1-\hat{x})\right)}{\Pi\hat{\lambda}_i\cosh\left(\Pi\hat{\lambda}_i\right)} & |\hat{x}|\ge\frac{R\theta}{L}\end{cases}$$

And the membrane strains are:

$$\epsilon = \frac{h_1+h_2}{R}\sum_{i=2}^{N+1} f_i'(x)\frac{\hat{\mathbf{b}}\cdot\hat{\mathbf{v}}_i}{\hat{\lambda}_i^2}\hat{\mathbf{v}}_i. \tag{17}$$

$$f_i'(\hat{x}) = \begin{cases} 1 - \dfrac{\cosh\left(\Pi\hat{\lambda}_i\frac{L_1}{L}\right)\cosh\left(\Pi\hat{\lambda}_i\hat{x}\right)}{\cosh\left(\Pi\hat{\lambda}_i\right)} & |\hat{x}| > \frac{R\theta}{L} \\ \dfrac{\sinh\left(\Pi\hat{\lambda}_i\frac{R\theta}{L}\right)\sinh\left(\Pi\hat{\lambda}_i(1-\hat{x})\right)}{\cosh\left(\Pi\hat{\lambda}_i\right)} & |\hat{x}| \geq \frac{R\theta}{L} \end{cases}$$

The membrane strain is further normalized by $N(h_1+h_2)/R$, which is the maximum membrane strain predicted by the Euler–Bernoulli beam theory:

$$\hat{\epsilon} = \frac{1}{N}\sum_{i=2}^{N+1} f_i'(x)\frac{\hat{\mathbf{b}}\cdot\hat{\mathbf{v}}_i}{\hat{\lambda}_i^2}\hat{\mathbf{v}}_i. \tag{18}$$

2.1.2. Case II: conforming to two arcs

Consider the deformation where the beam is conformed to two arcs of radius R_1 and R_2 lying on opposite sides of the beam, which is a common deformation in the roll-to-roll process. The curvature of the deformed shape is described as:

$$\kappa = \begin{cases} \frac{1}{R_1} & -1 \leq \hat{x} \leq \frac{R_1\theta_1}{L} - 1 \\ -\frac{1}{R_2} & \frac{R_1\theta_1}{L} - 1 \leq \hat{x} \leq 1 \end{cases} \tag{19}$$

Again, we focus on the case where all stiff layers have the same modulus E_h, Poisson's ratio ν_h, and height h_h, and all soft layers have the same shear modulus G_s and height h_s.

Plugging Eqs. (12), (15), and (19) into Eq. (11) and assuming $R_1\theta_1 \geq R_2\theta_2$ we have:

$$\mathbf{u} = \left(h_1+h_2\right)\sum_{i=2}^{N+1} F_i(x)\frac{\hat{\mathbf{b}}\cdot\hat{\mathbf{v}}_i}{\hat{\lambda}_i^2}\hat{\mathbf{v}}_i. \tag{20}$$

$$F_i(\hat{x}) = \begin{cases} \dfrac{\hat{x}}{R_1} + A_{i,1}\sinh\left(\Pi\hat{\lambda}_i\hat{x}\right) + A_{i,2}\cosh\left(\Pi\hat{\lambda}_i\hat{x}\right) & \hat{x} \leq \hat{x}_m \\ \dfrac{\hat{x}_m}{R_1} - \dfrac{\hat{x}-\hat{x}_m}{R_2} + A_{i,3}\sinh\left(\Pi\hat{\lambda}_i\hat{x}\right) + & \\ A_{i,4}\cosh\left(\Pi\hat{\lambda}_i\hat{x}\right) & \hat{x} \geq \hat{x}_m \end{cases}$$

where $\hat{x}_m = \frac{R_1\theta_1 - L}{L}$ is the position that the two arcs join, and $A_{i,1}, A_{i,2}, A_{i,3}, A_{i,4}$ are coefficients expressed as:

$$A_{i,1} = \frac{-(\frac{1}{R_1}+\frac{1}{R_2})\cosh\left(\Pi\hat{\lambda}_i(1-\hat{x}_m)\right) - \frac{1}{R_1} + \frac{1}{R_2}}{2\Pi\hat{\lambda}_i\cosh\left(\Pi\hat{\lambda}_i\right)}$$

$$A_{i,2} = \frac{-(\frac{1}{R_1}+\frac{1}{R_2})\cosh\left(\Pi\hat{\lambda}_i(1-\hat{x}_m)\right) + \frac{1}{R_1} + \frac{1}{R_2}}{2\Pi\hat{\lambda}_i\sinh\left(\Pi\hat{\lambda}_i\right)}$$

$$A_{i,3} = \frac{(\frac{1}{R_1}+\frac{1}{R_2})\cosh\left(\Pi\hat{\lambda}_i(1+\hat{x}_m)\right) - \frac{1}{R_1} + \frac{1}{R_2}}{2\Pi\hat{\lambda}_i\cosh\left(\Pi\hat{\lambda}_i\right)}$$

$$A_{i,4} = -\frac{-(\frac{1}{R_1}+\frac{1}{R_2})\cosh\left(\Pi\hat{\lambda}_i(1+\hat{x}_m)\right) + \frac{1}{R_1} + \frac{1}{R_2}}{2\Pi\hat{\lambda}_i\sinh\left(\Pi\hat{\lambda}_i\right)}$$

and the membrane strains are:

$$\epsilon = \left(h_1+h_2\right)\sum_{i=2}^{N+1} F_i'(x)\frac{\hat{\mathbf{b}}\cdot\hat{\mathbf{v}}_i}{\hat{\lambda}_i^2}\hat{\mathbf{v}}_i. \tag{21}$$

$$F_i'(\hat{x}) = \begin{cases} \dfrac{1}{R_1} + A_{i,1}\Pi\hat{\lambda}_i\cosh\left(\Pi\hat{\lambda}_i\hat{x}\right) & \\ +A_{i,2}\Pi\hat{\lambda}_i\sinh\left(\Pi\hat{\lambda}_i\hat{x}\right) & \hat{x} \leq \hat{x}_m \\ -\dfrac{1}{R_2} + A_{i,3}\Pi\hat{\lambda}_i\cosh\left(\Pi\hat{\lambda}_i\hat{x}\right) & \\ +A_{i,4}\Pi\hat{\lambda}_i\sinh\left(\Pi\hat{\lambda}_i\hat{x}\right) & \hat{x} \geq \hat{x}_m \end{cases}$$

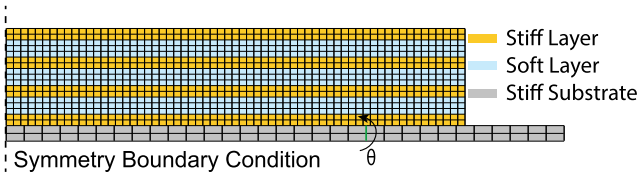


Fig. 5. A schematic of the FEA model set-up.

The membrane strains are normalized as:

$$\hat{\epsilon} = \frac{\min(R_1,R_2)}{N}\sum_{i=2}^{N+1} F_i'(x)\frac{\hat{\mathbf{b}}\cdot\hat{\mathbf{v}}_i}{\hat{\lambda}_i^2}\hat{\mathbf{v}}_i. \tag{22}$$

2.2. Numerical model

A finite element analysis was performed using the ABAQUS software package to validate the analytical results. The bottom surface of the laminated beam was attached to an extremely stiff substrate beam using a frictionless 'hard' contact that does not allow separation after contact (Fig. 5). The symmetry boundary condition was imposed on both the substrate and the laminated beam so that only the right half of the beam was analyzed. Rotation was applied on a selected cross-section of the substrate. The geometry of the system was discretized using a structured mesh consisting of CPE4R elements.

3. Result

The baseline geometrical parameters and material properties are chosen to be $2L$ = 10 mm, h_1 = 50 nm, h_2 = 1 μm, N = 6, E_1 = 79 GPa, ν_1 = 0.415, E_2 = 0.5 MPa, and ν_2 = 0.495 based on a typical neural probe (Le Floch et al., 2023). The loading condition, if not otherwise stated, is L_1 = 0 cm and R = 100 mm for case I, in which case the curvature is constant.

3.1. Position dependence

Fig. 6a plots the normalized membrane strains $\hat{\epsilon}$ along the stiff layers of the multilayer laminated beams according to Eq. (18), the Euler–Bernoulli beam theory, and FEA. The results from the proposed theory agree excellently with the FEA, while there is a significant deviation from the Euler–Bernoulli beam theory. In all layers, $\hat{\epsilon}$ increases from 0 at the two ends of the beam and reaches a plateau when $\hat{\epsilon} < 0.65$. At the plateau, the membrane strains of the proposed theory align with the predictions from the Euler–Bernoulli beam theory. This position-dependent deformation forms a distinct contrast to the Euler–Bernoulli beam theory, where the membrane strain is position-independent under a constant curvature. A Similar position-dependent membrane strain has also been reported by Li et al. (2016) for a trlayer beam. The small rotation angle of 0.05 rad applied in the numerical simulation effectively excludes the geometrical nonlinear effects around the beam edges as reported in Chen et al. (2023). When there is a large rotation in the deformed configuration, geometrical non-linearity needs to be included in the FEA simulation and the strain tensor needs to be transformed into longitudinal and normal directions in the deformed configuration.

The internal moment at a cross-section can be calculated from the membrane strains and the curvatures of the stiff layers as:

$$M = \sum_{k=1}^{N+1}\left(\overline{EI}_{2k-1}\kappa_{2k-1} + y_{2k-1}\overline{EA}_{2k-1}\epsilon_{2k-1}\right). \tag{23}$$

The contribution from the soft layers to the bending moment is neglected in Eq. (23) due to the extreme modulus mismatch. We define the equivalent flexural rigidity to be:

$$D = \frac{M}{\kappa} = MR \tag{24}$$

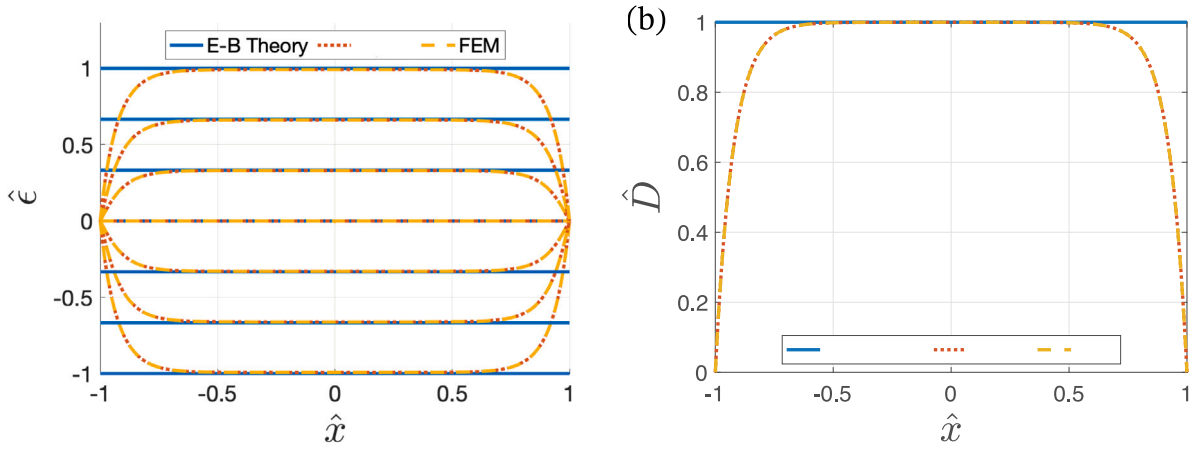


Fig. 6. (a) The normalized membrane strain and (b) the normalized equivalent flexural rigidity along the beam under constant curvature. Both are position dependent.

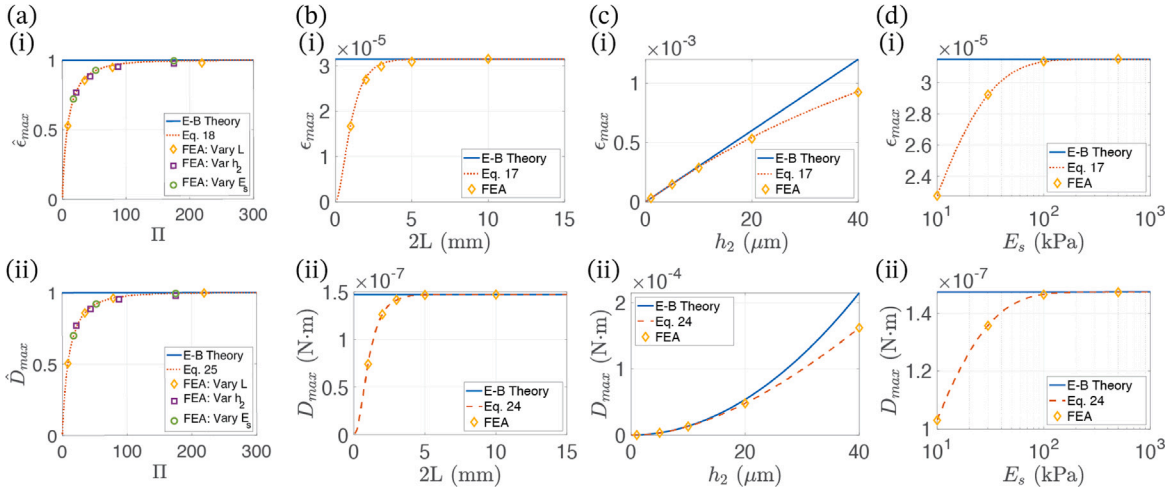


Fig. 7. (a) The master curves depicting (i) the increase in normalized maximum membrane strain $\hat{\epsilon}_{max}$ and (ii) the increase in normalized maximum flexural rigidity $\hat{D}_{max}$ as the shear-lag number Π enlarges. (b) (i) The maximum membrane strain ϵ_{max} and (ii) the maximum flexural rigidity D_{max} increase with the beam length $2L$ and approach the Euler–Bernoulli beam theory. (c) (i) The maximum membrane strain ϵ_{max} and (ii) the maximum flexural rigidity D_{max} increase with the soft layer thickness h_2 and diverge from the Euler–Bernoulli beam theory as soft layer becomes thicker. (d) (i) The maximum membrane strain ϵ_{max} and (ii) the maximum flexural rigidity D_{max} increase with the soft layer modulus E_2 and converge to the Euler–Bernoulli beam theory.

The equivalent flexural rigidity is further normalized by the flexural rigidity predicted by the Euler–Bernoulli beam theory D_{EB} to be:

$$\hat{D} = \frac{D}{D_{\mathrm{EB}}} \tag{25}$$

Fig. 6b plots the normalized equivalent flexural rigidity against the normalized x coordinate for the baseline case. $\hat{D}$ starts from 0.000047 at two ends and increases towards a plateau in the middle region. The $\hat{D}$ reaches a peak of 0.9999 at $\hat{x} = 0$. The observed position dependence of $\hat{D}$ closely resembles that of $\hat{\epsilon}$, as the bending moment is calculated from the membrane strains.

3.2. Effect of the shear-lag number Π

In this section, the effect of the shear-lag number Π is systematically investigated for the case N = 6 by varying the beam length, soft layer thickness, and soft layer modulus. These parameters can be adjusted conveniently in the fabrication process. For conciseness, we only plot the maximum normalized membrane strain $\hat{\epsilon}_{max}$ and the maximum normalized flexural rigidity $\hat{D}_{max}$, which is the $\hat{\epsilon}$ and $\hat{D}$ of the topmost layer when $\hat{x} = 0$. Fig. 7a plots the master curve of $\hat{\epsilon}_{max}$ and $\hat{D}_{max}$ versus Π. $\hat{\epsilon}_{max}$ begins at 0 and approaches 1 as Π increases, indicating that the shear-lag effect diminishes at a large shear-lag number and the shear-lag theory converges to the classical Euler–Bernoulli beam theory. A similar trend is observed for $\hat{D}_{max}$.

Fig. 7b–d plot the maximum membrane strain ϵ_{max} and the maximum flexural rigidity D_{max} predicted by Eqs. (17) and (24) versus the beam length $2L$, the soft layer height h_2, and the soft layer modulus E_s. The results are compared to the Euler–Bernoulli theory and FEA. The proposed shear-lag theory matches excellently with FEA for all parameters investigated.

While the Euler–Bernoulli beam theory predicts a length-independent membrane strain and flexural rigidity, the proposed shear-lag theory predicts that both ϵ_{max} and D_{max} increase with beam length and approaches the Euler–Bernoulli beam theory when L is large enough (Fig. 7b). The observed length dependence is a result of increasing aspect ratio as beam length increases, which in turn enlarges the shear-lag number Π and attenuates the shear-lag effect.

Both the shear-lag theory and the Euler–Bernoulli beam theory predict increasing ϵ_{max} and D_{max} as the soft layer thickens. However, the discrepancy between the two becomes more pronounced at larger soft layer thickness (Fig. 7c). The increasing deviation results from decreasing Π as the soft layer aspect ratio decreases, strengthening the shear-lag effect. For the cases studied, the increasing shear-lag effect

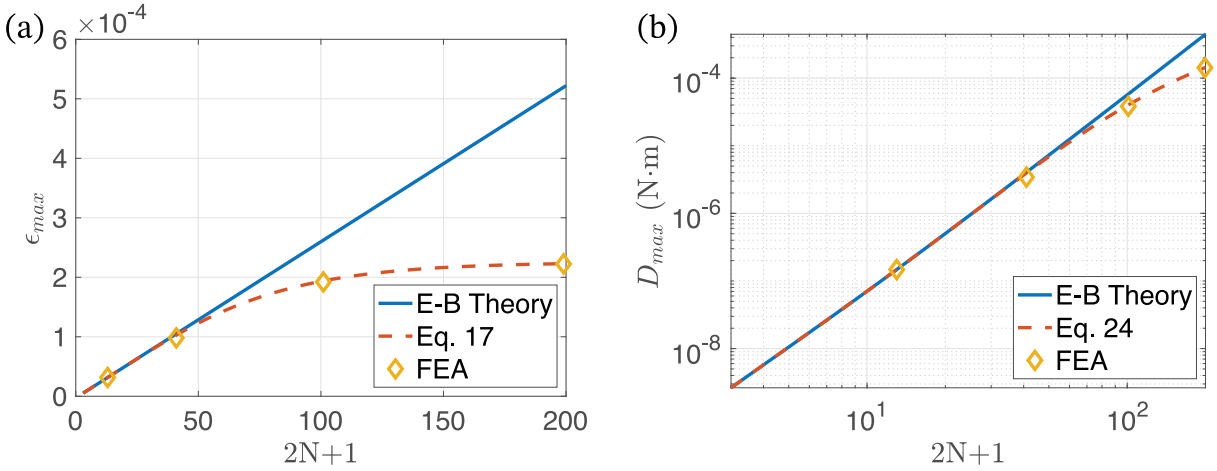


Fig. 8. (a) The maximum membrane strain ϵ_{max} and (b) the maximum flexural rigidity D_{max} increase with layer number 2N + 1.

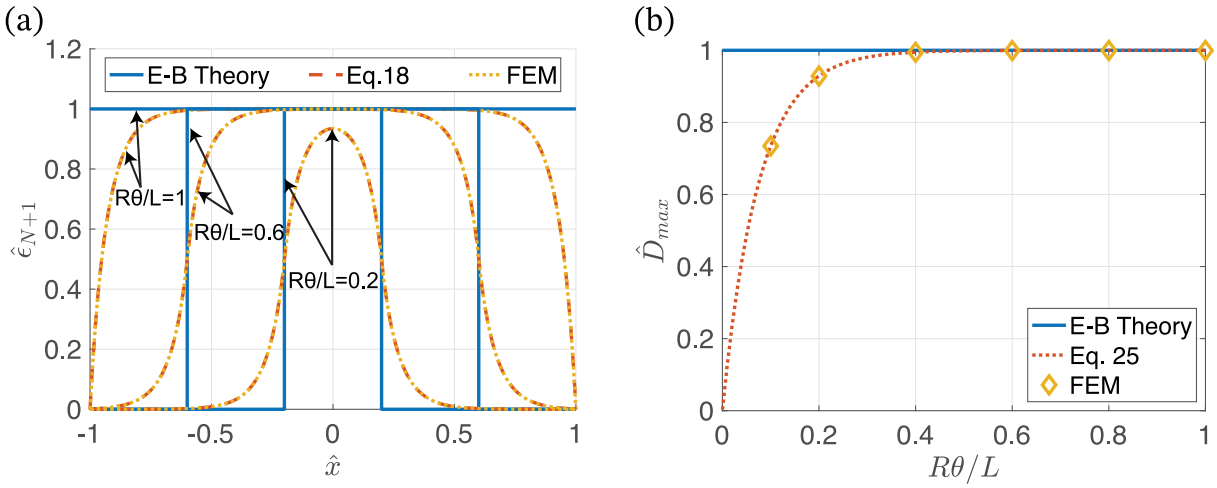


Fig. 9. (a) The membrane strain in the topmost layer along the beam length when the beam conforms to a rounded wedge. (b) The maximum equivalent flexural rigidity increases with the normalized deformed area $R\theta/L$.

is overridden by the increasing cross-sectional area, and therefore ϵ_{max} and D_{max} still increase with increasing h_2.

Similar to the case of the beam length, both ϵ_{max} and D_{max} increase with the soft layer modulus E_2 and converge to the Euler–Bernoulli beam theory (Fig. 7d). This is consistent with the fact decreasing modulus mismatch lowers Π and inhibits the shear-lag effect. Notice that the dependence of flexural rigidity on E_2 in the Euler–Bernoulli beam theory is negligible due to the extreme modulus mismatch (Fig. 7d(ii)).

3.3. Effect of the layer number

We investigate the effect of the layer number by changing N from 1 to 100 while maintaining a constant Π (Fig. 8). The proposed shear-lag theory agrees excellently with the FEA results, with the maximum error being less than 0.2%. Both the shear-lag theory and the Euler–Bernoulli theory predict an increase in maximum membrane strain and maximum flexural rigidity as the total thickness of the laminated beam increases with the layer number. For the selected parameters, the difference between the two theories is less than 0.1% for both ϵ_{max} and D_{max} when N = 1. The discrepancy grows as N increases. When N = 100, the ϵ_{max} and D_{max} predicted by the shear-lag theory is only 42.5% and 32.7% of the prediction by the Euler–Bernoulli beam theory respectively. This indicates that the shear-lag effect accumulates as the number of soft layers increases.

3.4. Effect of the deformed shape

In this section, we investigate the effect of deformed shape and keep the beam properties the same as the baseline case for two categories of deformation. For case I where the beam conforms to a round wedge, we vary the bending area $R\theta$ while keeping the $R = 100$ mm. For case II where the beam conforms to cylinders on the opposite side of the beam as in roll to roll processing, we first vary $\hat{x}_m$ while keeping $R_1 = R_2 = 100$ mm; we then vary the ratio of the radius of two arcs R_2/R_1 while keeping $R_1 = 100$ mm and $\hat{x}_m = 0$.

3.4.1. Conforming to round wedge

Fig. 9a illustrates the normalized membrane strain along the topmost layer $\hat{\epsilon}_{N+1}$ for various $R\theta/L$. The shear-lag theory matches perfectly with FEA for all cases examined. While the Euler–Bernoulli beam theory predicts a step-like membrane strain in accordance with the applied curvature, the shear-lag theory predicts a smooth, S-shaped change in membrane strain near the curvature discontinuity. The membrane strain peaks at $\hat{x} = 0$ for all cases. The peak value aligns closely with the Euler–Bernoulli beam theory when $R\theta/L = 1$ and $R\theta/L = 0.6$, while there is a difference of 6.5% for $R\theta/L = 0.2$. For all $\hat{x}$ values, $\hat{\epsilon}_{N+1}$ increases with increasing bent area $R\theta/L$.

Notice that the membrane strains are finite when the local curvature is zero for cases where $R\theta/L < 1$. Correspondingly, the internal bending moment could also be finite when curvature is zero. To avoid dividing

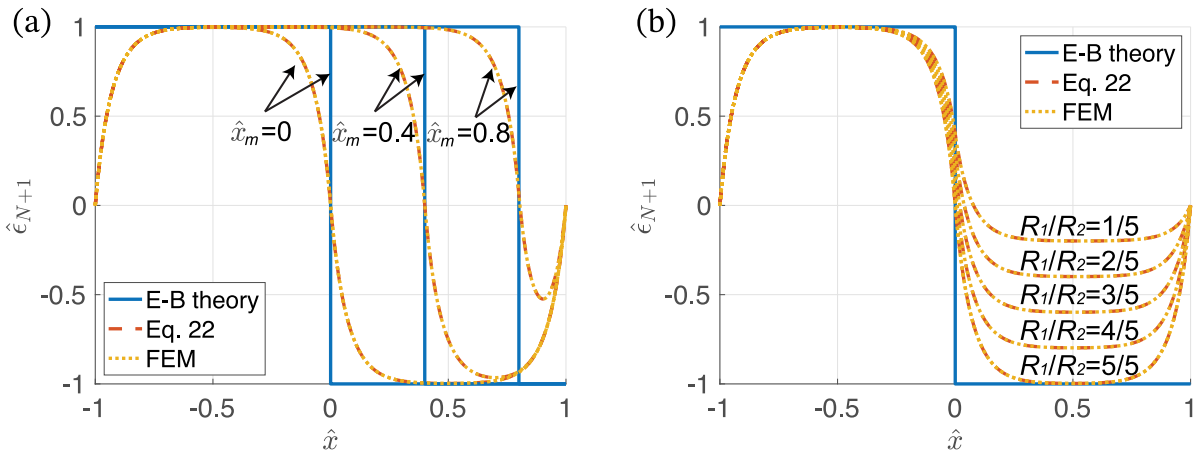


Fig. 10. The normalized membrane strain along the topmost layer of the beam when conforming to two cylinders (a) of the same radius and varying arc lengths and (b) of the same arc length and varying radius.

finite internal moment by zero curvature, we define the equivalent flexural rigidity in the general case as:

$$D(x,\kappa(x)) = \frac{|M(x)|}{\max(|\kappa|)}. \tag{26}$$

In this case, $\max(|\kappa|) = 1/R$. The normalized equivalent flexural rigidity is defined as dividing $D(x,\kappa(x))$ by the flexural rigidity predicted by the Euler–Bernoulli beam theory:

$$\hat{D}(x,\kappa(x)) = \frac{D(x,\kappa(x))}{D_{EB}}. \tag{27}$$

Fig. 9b plots the maximum normalized flexural rigidity $\hat{D}_{max}$ against the normalized bent area $R\theta/L$. The maximum normalized flexural rigidity starts at 0 and approaches the 1 as $R\theta/L$ increases. $\hat{D}_{max}$ reaches the maximum when $R\theta/L = 1$, i.e., when the entire beam is subjected to a constant curvature.

3.4.2. Conforming to two cylinders

Fig. 10a plots the normalized membrane strain along the topmost layer for $\hat{x}_m = 0, 0.4, 0.8$ when $R_1 = R_2$ along with the Euler–Bernoulli theory and the finite element simulations. Similar to case I, the normalized strains predicted by the shear-lag theory exhibit smooth changes around the curvature jumps in contrast to the step-like change predicted by the Euler–Bernoulli beam theory. When $\hat{x} = 0$, the result is anti-symmetric, with the normalized strain being zero at two ends and $\hat{x} = 0$, and approaching ± 1 when $|\hat{x}|$ is around 0.5. As the $\hat{x}_m$ increases, the symmetry breaks down. The magnitude of membrane strain decreases in areas conforming to the 2nd cylinder, indicating a stronger shear-lag effect due to decreased equivalent length $R_2\theta_2$.

Fig. 10b plots the normalized membrane strain along the topmost layer for $R2/R1 = 1, \frac{5}{4}, \frac{5}{3}, \frac{5}{2}, 5$. Again, a smooth change is observed at the curvature jump. Varying curvature at $\hat{x} > 0$ has some influence on the membrane strains when $\hat{x} < 0$ due to the non-local nature of shear-lag effect. However, the effect quickly diminishes after $\hat{x} < -0.25$ for the parameter chosen.

4. Discussion

4.1. Upper bound of the flexural rigidity

Section 3.4 showed that the equivalent flexural rigidity depends on the applied bending curvature $\kappa(x)$. In this section, we further show that the equivalent flexural rigidity reaches the maximum for a given laminated beam when the beam is under constant curvature.

Consider a beam subject to a given bending curvature $\kappa(x)$. Denote $\kappa_M = \max(\kappa)$, $\kappa_m = \min(\kappa)$. Without the loss of generosity, assume that $\kappa_M > |\kappa_m| \geq 0$. Combining equations Eqs. (13), (23), and (26), we have:

$$\begin{aligned}
D(x,\kappa(x)) =& \frac{h_1+h_2}{\kappa_M}\sum_{i=2}^{N+1}\left[\sinh\Pi\hat{\lambda}_i(1-\hat{x})\int_0^{\hat{x}}\left(\kappa^{\mathrm{S}}(s)\frac{\cosh\Pi\hat{\lambda}_i s}{\cosh\Pi\hat{\lambda}_i}\right.\right.\\
&\left.+\kappa^{\mathrm{A}}(s)\frac{\sinh\left(\Pi\hat{\lambda}_i s\right)}{\sinh\Pi\hat{\lambda}_i}\right)ds+\int_{\hat{x}}^{1}\left(\kappa^{\mathrm{S}}(s)\frac{\cosh\Pi\hat{\lambda}_i\hat{x}}{\cosh\Pi\hat{\lambda}_i}+\right.\\
&\left.\left.\kappa^{\mathrm{A}}(s)\frac{\sinh\Pi\hat{\lambda}_i\hat{x}}{\sinh\Pi\hat{\lambda}_i}\right)\sinh\Pi\hat{\lambda}_i(1-s)ds\right]\frac{\Pi g_i\hat{\mathbf{v}}_i\cdot\mathbf{y}}{\hat{\lambda}_i}\\
&+(N+1)\overline{EI}_1\frac{\kappa}{\kappa_M}\\
\leq&\frac{h_1+h_2}{\kappa_M}\sum_{i=2}^{N+1}\left[\sinh\Pi\hat{\lambda}_i(1-\hat{x})\int_0^{\hat{x}}\kappa_M\frac{\cosh\Pi\hat{\lambda}_i s}{\cosh\Pi\hat{\lambda}_i}ds+\right.\\
&\left.\int_{\hat{x}}^{1}\kappa_M\frac{\cosh\Pi\hat{\lambda}_i\hat{x}}{\cosh\Pi\hat{\lambda}_i}\sinh\Pi\hat{\lambda}_i(1-s)ds\right]\frac{\Pi g_i\hat{\mathbf{v}}_i\cdot\mathbf{y}}{\hat{\lambda}_i}\\
&+(N+1)\overline{EI}_1\\
=&D(x,\kappa(x)=\kappa_M)\\
=&D^{arc}(x)
\end{aligned} \tag{28}$$

Notice that $D^{arc}(x)$ is independent of the applied bending curvature. $D^{arc}(x)$ can be used to estimate the maximum bending moments of the laminated beam for the applications where the deformed shape is known, for example, bio-electronics conforming to human bodies.

4.2. The limiting case of extremely small Π and large Π

In Section 3.2, we demonstrated numerically that the proposed theory approaches the Euler–Bernoulli beam theory at large Π for the investigated deformations. We can further establish this mathematically for any layer number and applied bending curvature $\kappa(x)$ (Appendix C). Note that $\Pi^2 = \left(1-\nu_1^2\right)\frac{L^2}{h_1h_2}\frac{G_2}{E_1}$ is the product of the soft layer aspect ratio, stiff layer aspect ratio, and modulus mismatch. This indicates that a lower modulus mismatch and higher aspect ratio inhibit the shear-lag effect, which is common in many shear-lag problems (Cox, 1952; Reissner, 1938).

It can be easily proved that $\lim_{\Pi->0}\mathbf{u} = 0$ in Eq. (11). Therefore we have $\lim_{\Pi->0}\boldsymbol{\epsilon} = 0$ and $\lim_{\Pi->0} D = (N+1)\overline{EI}_1$. This indicates that when Π is sufficiently small, the stiff layers become decoupled and the flexural rigidity of the beam is solely the algebraic sum of the flexural rigidity of the stiff layers. This extreme case corresponds to $G_2 = 0$ and represents the lower bound of the flexural rigidity of the laminated beam, where the stiff layers can slide upon each other freely like pages in a book.

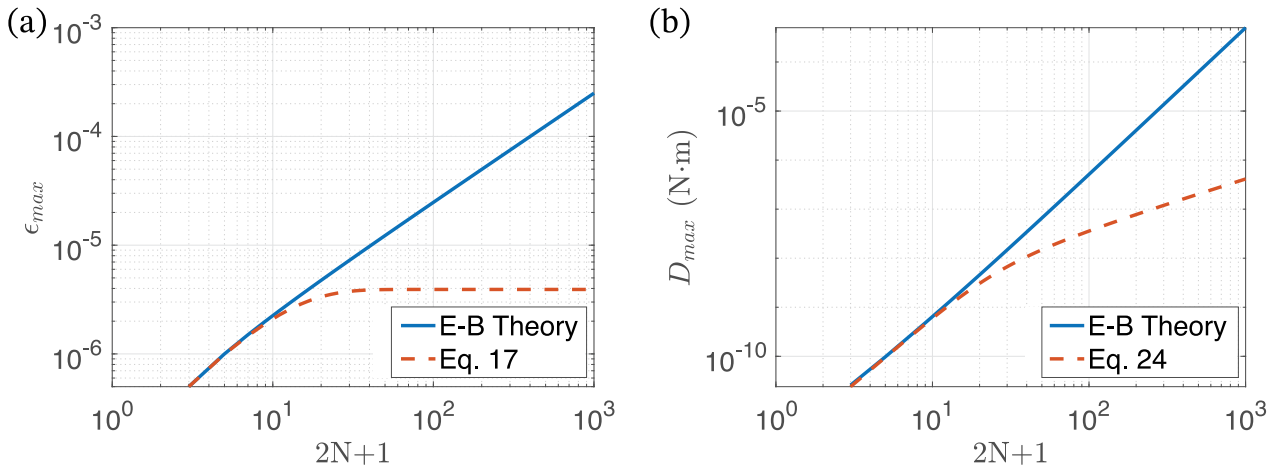


Fig. 11. (a) The maximum membrane strain reaches a plateau at large layer number. (b) The flexural rigidity scales linearly with the layer number at large layer number.

4.3. The extreme case of N approaches infinity

In this section, we investigate the limiting case as N tends to infinity. To exhibit the trend when N is sufficiently large while maintaining the slender aspect ratio of the laminated beam, we change E_2 to 0.1 MPa and h_2 to 50 nm and keep the remaining parameters unchanged. Fig. 11 illustrates the maximum membrane strain and the maximum flexural rigidity of the proposed theory in comparison to the Euler–Bernoulli beam theory. Interestingly, the maximum membrane strain reaches a plateau as the layer number increases, in contrast to the linear increase predicted by the Euler–Bernoulli beam theory. This observation indicates that, with careful design consideration, the multilayer laminated beam can be scaled up without the risk of brittle functional members failing due to bending.

Here, we present a mathematical proof that ϵ_{max} is bounded. The membrane strains are written as:

$$\boldsymbol{\epsilon} = \frac{h_1+h_2}{R}\sum_{i=2}^{N+1}\left[1-\frac{\cosh\left(\hat{\lambda}_i\Pi\hat{x}\right)}{\cosh\left(\hat{\lambda}_i\Pi\right)}\right]\frac{\hat{\mathbf{v}}_i\cdot\hat{\mathbf{b}}}{\hat{\lambda}_i^2}\hat{\mathbf{v}}_i \tag{29}$$

Let

$$\mathbf{V} = [\hat{\mathbf{v}}_1, \hat{\mathbf{v}}_2, \hat{\mathbf{v}}_3, \ldots, \hat{\mathbf{v}}_{N+1}] \tag{30}$$

be the matrix formed by the unit eigenvectors of $\hat{\mathbf{C}}\hat{\mathbf{A}}$. Notice that $\mathbf{V}$ is orthogonal because $\hat{\mathbf{C}}\hat{\mathbf{A}}$ is symmetric for the case considered. Let $\epsilon_0 = \frac{h_1+h_2}{R}$, $k_i = \left[1-\frac{1}{\cosh(\hat{\lambda}_i\Pi)}\right]\frac{1}{\hat{\lambda}_i^2}$. Easy to show, $0 < k_i < \Pi^2$, and we have:

$$\begin{aligned}
\epsilon_{max} &= |\epsilon_{N+1}(0)| \\
&= \left|\epsilon^0\sum_{i=2}^{N+1}k_i\hat{\mathbf{v}}_i\cdot\hat{\mathbf{b}}V_{i,N+1}\right| \\
&= \left|\epsilon^0\sum_{i=2}^{N+1}k_i\left(V_{i,N+1}^2 - V_{i,N+1}V_{i,1}\right)\right| \\
&\le \epsilon^0\sum_{i=2}^{N+1}k_i\left(V_{i,N+1}^2 + |V_{i,N+1}|\,|V_{i,1}|\right) \\
&\le \epsilon^0\Pi^2\sum_{i=2}^{N+1}\left(V_{i,N+1}^2 + |V_{i,N+1}|\,|V_{i,1}|\right) \\
&\le 2\Pi^2\epsilon^0
\end{aligned} \tag{31}$$

Consistent with the constant maximum membrane strain at a large layer number, the flexural rigidity scales linearly with the layer number instead of following the cubic relationship predicted by the Euler–Bernoulli beam theory (Fig. 11). This is especially important for applications like neural probes where both softness and the channel numbers are desired.

5. Conclusions

In this study, we formulated a comprehensive framework to analyze multilayer laminated beams with extreme modulus mismatch under various bending conditions. We validated our theory through FEA. We discerned a unique control parameter that reflects the interplay between modulus mismatch and the aspect ratio, which in turn determines the deviations from the Euler–Bernoulli beam theory. Furthermore, we introduced a position and deformation-dependent equivalent flexural rigidity. We discovered that while the flexural rigidity exhibits a power-law dependence on the number of layers, the membrane strain approaches a plateau and its upper bound is revealed.

CRediT authorship contribution statement

Zheliang Wang: Conceptualization, Methodology, Software, Validation, Investigation, Writing – original draft, Writing – review & editing. **Hao Sheng:** Conceptualization, Writing – review & editing. **Xinyi Lin:** Conceptualization, Writing – review & editing. **Yifan Rao:** Writing – review & editing. **Jia Liu:** Conceptualization, Writing – review & editing, Supervision. **Nanshu Lu:** Conceptualization, Writing – review & editing, Supervision.

Declaration of competing interest

The authors declare that they have no known competing financial interests or personal relationships that could have appeared to influence the work reported in this paper.

Data availability

Data will be made available on request.

Declaration of Generative AI and AI-assisted technologies in the writing process

During the preparation of this work the authors used ChatGPT in order to polish the language. After using this tool, the authors reviewed and edited the content as needed and take(s) full responsibility for the content of the publication.

Appendix A. Eigenvalues of matrix $\hat{\mathbf{C}}\hat{\mathbf{A}}$

It is easy to check that $\hat{\mathbf{C}}$ and $\hat{\mathbf{C}}^{-1}$ are positive-definite symmetric matrices and that $\hat{\mathbf{A}}$ is a symmetric matrix. Moreover, it can be shown that $\hat{\mathbf{A}}$ is a positive semi-definite matrix. Let $\mathbf{w} = \left(w_1, w_2, \ldots, w_{N+1}\right)^T$ be a random N + 1 dimensional non-zero vector, we have:

$$\begin{aligned}\mathbf{w}^T\hat{\mathbf{A}}\mathbf{w} &= \sum_{i=1}^{N+1} w_i^2\hat{A}_{i,i} + \sum_{i=1}^{N} w_i w_{i+1}\left(\hat{A}_{i,i+1} + \hat{A}_{i+1,i}\right)\\ &= \frac{h_2}{G_2}\sum_{i=1}^{N}\frac{G_{2i}}{h_{2i}}\left[w_i - w_{i+1}\right]^2\\ &\geq 0,\end{aligned} \tag{32}$$

The equal sign only holds when $\mathbf{w}$ is colinear with $(1,1,1,\ldots,1)^T$, i.e., the nullity of $\hat{\mathbf{A}}$ is 1. Utilizing the rank-nullity theorem and the fact that $\hat{\mathbf{C}}$ is full rank, we have $\hat{\mathbf{C}}\hat{\mathbf{A}}$ has only one zero eigenvalue.

Let λ be an arbitrary nonzero eigenvalue of $\hat{\mathbf{C}}\hat{\mathbf{A}}$ and $\mathbf{v}$ be the corresponding eigenvector, we have:

$$\begin{aligned}\lambda\mathbf{v}^*\hat{\mathbf{C}}^{-1}\mathbf{v} &= \mathbf{v}^*\hat{\mathbf{C}}^{-1}\hat{\mathbf{C}}\hat{\mathbf{A}}\mathbf{v} = \mathbf{v}^*\hat{\mathbf{A}}^*\mathbf{v} = \mathbf{v}^*\hat{\mathbf{A}}^*\hat{\mathbf{C}}^*\hat{\mathbf{C}}^{*-1}\mathbf{v}\\ &= \lambda^*\mathbf{v}^*\hat{\mathbf{C}}^{-1}\mathbf{v}.\end{aligned} \tag{33}$$

Therefore,

$$(\lambda - \lambda^*)\mathbf{v}^*\hat{\mathbf{C}}^{-1}\mathbf{v} = 0. \tag{34}$$

Notice that $\mathbf{v}^*\hat{\mathbf{C}}^{-1}\mathbf{v} > 0$ because $\hat{\mathbf{C}}^{-1}$ is positive definitive, we have $\lambda = \lambda^*$, i.e., any eigenvalue of $\hat{\mathbf{C}}\hat{\mathbf{A}}$ are real.

Now, let $\lambda_i^{\hat{\mathbf{A}}}, i = 1,2,\ldots,n$ be the eigenvalues of $\hat{\mathbf{A}}$ in ascending order and $\mathbf{v}_i^{\hat{\mathbf{A}}}$ be the corresponding unit eigenvectors. $\mathbf{v}_i^{\hat{\mathbf{A}}}$ forms an orthogonal base because $\hat{\mathbf{A}}$ is symmetric. Therefore, $\mathbf{v} = \sum_{i=1}^{i=N+1}(\mathbf{v}\cdot\mathbf{v}_i^{\hat{\mathbf{A}}})\mathbf{v}_i^{\hat{\mathbf{A}}}$. And we have:

$$\lambda = \frac{\hat{\mathbf{A}}\mathbf{v}\cdot\hat{\mathbf{C}}\hat{\mathbf{A}}\mathbf{v}}{\hat{\mathbf{A}}\mathbf{v}\cdot\mathbf{v}} = \frac{\left(\hat{\mathbf{A}}\mathbf{v}\right)^T\hat{\mathbf{C}}\left(\hat{\mathbf{A}}\mathbf{v}\right)}{\sum_{i=2}^{i=N+1}(\mathbf{v}\cdot\mathbf{v}_i^{\hat{\mathbf{A}}})^2\lambda_i^{\hat{\mathbf{A}}}} > 0. \tag{35}$$

which concludes the proof that $\hat{\mathbf{C}}\hat{\mathbf{A}}$ has one zero eigenvalue and N positive eigenvalues.

Appendix B. Decomposition of $\hat{\mathbf{C}}\mathbf{b}$ in the eigenspace of $\hat{\mathbf{C}}\hat{\mathbf{A}}$

Let $\lambda_i^{\hat{\mathbf{A}}}$ be the eigenvalues of $\hat{\mathbf{A}}$ in ascending order and $\mathbf{v}_i^{\hat{\mathbf{A}}}$ be the corresponding unit eigenvector. As shown in Appendix A, $\lambda_1^{\hat{\mathbf{A}}} = 0$, $\lambda_2^{\hat{\mathbf{A}}} > 0$, $\mathbf{v}_i^{\hat{\mathbf{A}}}\cdot\mathbf{v}_j^{\hat{\mathbf{A}}} = \delta_{ij}$. We can decompose $\hat{\mathbf{b}}$ in the eigenspace of $\hat{\mathbf{A}}$ as:

$$\hat{\mathbf{b}} = \sum_{i=1}^{N+1}(\hat{\mathbf{b}}\cdot\mathbf{v}_i^{\hat{\mathbf{A}}})\mathbf{v}_i^{\hat{\mathbf{A}}}$$

It can be shown that $\mathbf{v}_1^{\hat{\mathbf{A}}} = \frac{1}{\sqrt{N+1}}(1,1,1,\ldots,1)^T$ and that $\mathbf{v}_1^{\hat{\mathbf{A}}}\cdot\hat{\mathbf{b}} = 0$. Therefore,

$$\hat{\mathbf{b}} = \sum_{i=2}^{N+1}(\hat{\mathbf{b}}\cdot\mathbf{v}_i^{\hat{\mathbf{A}}})\mathbf{v}_i^{\hat{\mathbf{A}}} = \hat{\mathbf{A}}\sum_{i=2}^{i=N}\frac{\mathbf{b}\cdot\mathbf{v}_i^{\hat{\mathbf{A}}}}{\lambda_i^{\hat{\mathbf{A}}}}\mathbf{v}_i^{\hat{\mathbf{A}}} = \hat{\mathbf{A}}\mathbf{y}$$

Let λ_i be the eigenvalues of $\hat{\mathbf{C}}\hat{\mathbf{A}}$ in ascending order and $\mathbf{v}_i$ be the corresponding unit eigenvectors. As shown in Appendix A, $\lambda_1 = 0$, $\lambda_2 > 0$. Decompose $\mathbf{y}$ in the eigenspace of $\hat{\mathbf{C}}\hat{\mathbf{A}}$ as:

$$\mathbf{y} = \sum_{i=1}^{N+1} h_i\mathbf{v}_i.$$

Utilizing $\hat{\mathbf{b}} = \hat{\mathbf{A}}\mathbf{y}$ and $\lambda_1 = 0$, we have:

$$\hat{\mathbf{C}}\hat{\mathbf{b}} = \hat{\mathbf{C}}\hat{\mathbf{A}}\mathbf{y} = \hat{\mathbf{C}}\hat{\mathbf{A}}\sum_{i=1}^{N+1} h_i\mathbf{v}_i = \sum_{i=2}^{N+1}\lambda_i h_i\mathbf{v}_i$$

This completes the proof that $\hat{\mathbf{C}}\mathbf{b} = \sum_{i=1}^{i=N+1} g_i\mathbf{v}_i$, $g_1 = 0$

Appendix C. Convergence of proposed theory with the Euler–Bernoulli theory at large Π

It suffices to show that the membrane strains converge with the Euler–Bernoulli beam theory at large Π. Combining Eq. (1) with Eq. (11), we have:

$$\begin{aligned}\epsilon =& (h_1+h_2)\sum_{i=2}^{N+1}\frac{\Pi\hat{\mathbf{b}}\cdot\hat{\mathbf{v}}_i}{\hat{\lambda}_i}\left[\int_0^{\hat{x}}\kappa^S(s)\left(\frac{\sinh\Pi\hat{\lambda}_i(1-\hat{x}+s)}{2\cosh\Pi\hat{\lambda}_i}\right.\right.\\ &+\left.\frac{\sinh\Pi\hat{\lambda}_i(1-x-s)}{2\cosh\Pi\hat{\lambda}_i}\right)ds + \int_0^{\hat{x}}\kappa^A(s)\left(\frac{\cosh\Pi\hat{\lambda}_i(1-x+s)}{2\sinh\Pi\hat{\lambda}_i}\right.\\ &-\left.\frac{\cosh\Pi\hat{\lambda}_i(1-x-s)}{2\sinh\Pi\hat{\lambda}_i}\right)ds + \int_{\hat{x}}^{1}\kappa^S(s)\left(\frac{\sinh\Pi\hat{\lambda}_i(1-s+x)}{2\cosh\Pi\hat{\lambda}_i}\right.\\ &+\left.\frac{\sinh\Pi\hat{\lambda}_i(1-x-s)}{2\cosh\Pi\hat{\lambda}_i}\right)ds + \int_{\hat{x}}^{1}\kappa^A(s)\left(\frac{\cosh\Pi\hat{\lambda}_i(1-x+s)}{2\sinh\Pi\hat{\lambda}_i}\right.\\ &-\left.\left.\frac{\cosh\Pi\hat{\lambda}_i(1-x-s)}{2\sinh\Pi\hat{\lambda}_i}\right)ds\right]\hat{\mathbf{v}}_i\end{aligned} \tag{36}$$

Utilizing the fact that:

$$\forall a > 0, \lim_{k->\infty}\int_0^a f(x)\frac{ke^{k(a-x)}}{e^k}dx = f(a) \tag{37}$$

We have:

$$\begin{aligned}\lim_{\Pi->\infty}\epsilon =& (h_1+h_2)\kappa\sum_{i=2}^{N+1}\frac{\hat{\mathbf{b}}\cdot\hat{\mathbf{v}}}{\hat{\lambda}_i^2}\hat{\mathbf{v}}_i\\ =& (h_1+h_2)\kappa\left[\frac{-N-1}{2},\frac{-N+1}{2},\ldots,\frac{N+1}{2}\right]^T.\end{aligned} \tag{38}$$

which is the membrane strain predicted by the Euler–Bernoulli beam theory.

References

Chen, Y., Liu, H., Pang, K., Zhang, C., Qin, H., Xu, Z., Liu, Y., 2023. Bending deformable tension-shear model for nacre-like composites. J. Mech. Phys. Solids 171, 105132.

Chen, X., Yi, C., Ke, C., 2015. Bending stiffness and interlayer shear modulus of few-layer graphene. Appl. Phys. Lett. 106 (10).

Chortos, A., Liu, J., Bao, Z., 2016. Pursuing prosthetic electronic skin. Nat. Mater. 15 (9), 937–950.

Cox, H., 1952. The elasticity and strength of paper and other fibrous materials. Br. J. Appl. Phys. 3 (3), 72.

Fan, H.-T., 1939. A Study of "Shear Lag" Phenomenon in a Stiffened Flat Panel by Photoelastic Methods (Ph.D. thesis). California Institute of Technology.

Gao, X.-L., Li, K., 2005. A shear-lag model for carbon nanotube-reinforced polymer composites. Int. J. Solids Struct. 42 (5–6), 1649–1667.

Geiger, S., Michon, J., Liu, S., Qin, J., Ni, J., Hu, J., Gu, T., Lu, N., 2020. Flexible and stretchable photonics: The next stretch of opportunities. ACS Photon. 7 (10), 2618–2635.

He, Z., Zhu, Y., Wu, H., 2022. A universal mechanical framework for noncovalent interface in laminated nanocomposites. Journal of the Mechanics and Physics of Solids 158, 104560.

Huang, R., 2020. Bending with slip. Nature Mater. 19 (3), 259–260.

Huang, Z., Hao, Y., Li, Y., Hu, H., Wang, C., Nomoto, A., Pan, T., Gu, Y., Chen, Y., Zhang, T., et al., 2018. Three-dimensional integrated stretchable electronics. Nat. Electron. 1 (8), 473–480.

Huang, Z., He, Z., Zhu, Y., Wu, H., 2023. A general theory for the bending of multilayer van der Waals materials. J. Mech. Phys. Solids 171, 105144.

Jackson, A., Vincent, J., Turner, R., 1989. A physical model of nacre. Compos. Sci. Technol. 36 (3), 255–266.

Ji, B., Gao, H., 2004. Mechanical properties of nanostructure of biological materials. J. Mech. Phys. Solids 52 (9), 1963–1990.

Jin, L., Yeager, M., Lee, Y.-J., O'Brien, D.J., Yang, S., 2022. Shape-morphing into 3D curved surfaces with nacre-like composite architectures. Sci. Adv. 8 (41), eabq3248.

Kuhn, P., 1939. A Recurrence Formula for Shear-Lag Problems. Technical Report.

Le Floch, P., Zhao, S., Liu, R., Molinari, N., Medina, E., Hao, S., Wang, Z., Kim, J., Sheng, H., Partarrieu, S., Wang, W., Tian, W., Sessler, C., Guogao, Z., Park, H., Gong, X., Spencer, A., Lee, J., Ye, T., Tang, X., Wang, X., Bertoldi, K., Lu, N., Kozinsky, B., Suo, Z., Liu, J., 2023. 3D spatiotemporally scalable in vivo neural probes based on fluorinated elastomers. Nature Nanotechnol. in press.

Lecomte, A., Descamps, E., Bergaud, C., 2018. A review on mechanical considerations for chronically-implanted neural probes. J. Neural Eng. 15 (3), 031001.

Lee, G.J., Choi, C., Kim, D.-H., Song, Y.M., 2018. Bioinspired artificial eyes: Optic components, digital cameras, and visual prostheses. Adv. Funct. Mater. 28 (24), 1705202.

Lee, T.-I., Jo, W., Kim, W., Kim, J.-H., Paik, K.-W., Kim, T.-S., 2019. Direct visualization of cross-sectional strain distribution in flexible devices. ACS Appl. Mater. Interfaces 11 (14), 13416–13422.

Li, S., Li, R., An, D., Wang, Y., Xu, X., Xue, R., Su, Y., 2022. Bioinspired staggered-array structure design for flexible batteries. Int. J. Solids Struct. 256, 111986.

Li, L., Lin, H., Qiao, S., Zou, Y., Danto, S., Richardson, K., Musgraves, J.D., Lu, N., Hu, J., 2014. Integrated flexible chalcogenide glass photonic devices. Nat. Photon. 8 (8), 643–649.

Li, S., Liu, X., Li, R., Su, Y., 2017. Shear deformation dominates in the soft adhesive layers of the laminated structure of flexible electronics. Int. J. Solids Struct. 110, 305–314.

Li, S., Su, Y., Li, R., 2016. Splitting of the neutral mechanical plane depends on the length of the multi-layer structure of flexible electronics. Proc. R. Soc. Lond. Ser. A Math. Phys. Eng. Sci. 472 (2190), 20160087.

Liu, D., Chen, W., Zhang, C., 2013. Improved beam theory for multilayer graphene nanoribbons with interlayer shear effect. Phys. Lett. A 377 (18), 1297–1300.

Liu, S., Rao, Y., Jang, H., Tan, P., Lu, N., 2022. Strategies for body-conformable electronics. Matter 5 (4), 1104–1136.

Luo, Y., Abidian, M.R., Ahn, J.-H., Akinwande, D., Andrews, A.M., Antonietti, M., Bao, Z., Berggren, M., Berkey, C.A., Bettinger, C.J., Chen, J., Chen, P., Cheng, W., Cheng, X., Choi, S.-J., Chortos, A., Dagdeviren, C., Dauskardt, R.H., Di, C.-a., Dickey, M.D., Duan, X., Facchetti, A., Fan, Z., Fang, Y., Feng, J., Feng, X., Gao, H., Gao, W., Gong, X., Guo, C.F., Guo, X., Hartel, M.C., He, Z., Ho, J.S., Hu, Y., Huang, Q., Huang, Y., Huo, F., Hussain, M.M., Javey, A., Jeong, U., Jiang, C., Jiang, X., Kang, J., Karnaushenko, D., Khademhosseini, A., Kim, D.-H., Kim, I.-D., Kireev, D., Kong, L., Lee, C., Lee, N.-E., Lee, P.S., Lee, T.-W., Li, F., Li, J., Liang, C., Lim, C.T., Lin, Y., Lipomi, D.J., Liu, J., Liu, K., Liu, N., Liu, R., Liu, Y., Liu, Y., Liu, Z., Liu, Z., Loh, X.J., Lu, N., Lv, Z., Magdassi, S., Malliaras, G.G., Matsuhisa, N., Nathan, A., Niu, S., Pan, J., Pang, C., Pei, Q., Peng, H., Qi, D., Ren, H., Rogers, J.A., Rowe, A., Schmidt, O.G., Sekitani, T., Seo, D.-G., Shen, G., Sheng, X., Shi, Q., Someya, T., Song, Y., Stavrinidou, E., Su, M., Sun, X., Takei, K., Tao, X.-M., Tee, B.C.K., Thean, A.V.-Y., Trung, T.Q., Wan, C., Wang, H., Wang, J., Wang, M., Wang, S., Wang, T., Wang, Z.L., Weiss, P.S., Wen, H., Xu, S., Xu, T., Yan, H., Yan, X., Yang, H., Yang, L., Yang, S., Yin, L., Yu, C., Yu, G., Yu, J., Yu, S.-H., Yu, X., Zamburg, E., Zhang, H., Zhang, X., Zhang, X., Zhang, X., Zhang, Y., Zhang, Y., Zhao, S., Zhao, X., Zheng, Y., Zheng, Y.-Q., Zheng, Z., Zhou, T., Zhu, B., Zhu, M., Zhu, R., Zhu, Y., Zhu, Y., Zou, G., Chen, X., 2023. Technology roadmap for flexible sensors. ACS Nano 17 (6), 5211–5295, PMID: 36892156.

Ma, X., Liu, L., Zhang, Z., Wei, Y., 2021. A method to determine the geometry-dependent bending stiffness of multilayer graphene sheets. J. Appl. Mech. 88 (1), 011004.

Minev, I.R., Musienko, P., Hirsch, A., Barraud, Q., Wenger, N., Moraud, E.M., Gandar, J., Capogrosso, M., Milekovic, T., Asboth, L., Torres, R.F., Vachicouras, N., Liu, Q., Pavlova, N., Duis, S., Larmagnac, A., Vörös, J., Micera, S., Suo, Z., Courtine, G., Lacour, S.P., 2015. Electronic dura mater for long-term multimodal neural interfaces. Science 347 (6218), 159–163.

Murasawa, G., Tohgo, K., Ishii, H., 2005. The effect of fiber volume fraction and aspect ratio on the creation of internal stress in the matrix and deformation for short-fiber shape memory alloy composite. Smart materials and structures 15 (1), 33.

Nairn, J.A., Mendels, D.-A., 2001. On the use of planar shear-lag methods for stress-transfer analysis of multilayered composites. Mech. Mater. 33 (6), 335–362.

Park, H.-L., Lee, Y., Kim, N., Seo, D.-G., Go, G.-T., Lee, T.-W., 2020. Flexible neuromorphic electronics for computing, soft robotics, and neuroprosthetics. Adv. Mater. 32 (15), 1903558.

Priya, C.B., Keerthana, M., Verma, M., Banjara, N.K., 2013. Design of steel channel tension members-proposal to IS 800: 2007. J. Struct. Eng. 38, 122–130.

Reissner, E., 1938. On the problem of stress distribution in wide-flanged box-beams. J. Aeronaut. Sci. 5 (8), 295–299.

Reissner, E., 1946. Analysis of shear lag in box beams by the principle of minimum potential energy. Q. Appl. Math. 4 (3), 268–278.

Shen, Y., Wu, H., 2012. Interlayer shear effect on multilayer graphene subjected to bending. Appl. Phys. Lett. 100 (10).

Shi, Y., Rogers, J.A., Gao, C., Huang, Y., 2014. Multiple neutral axes in bending of a multiple-layer beam with extremely different elastic properties. J. Appl. Mech. 81 (11), 114501.

Singh, G.J., Mandal, S., Kumar, R., Kumar, V., 2020. Simplified analysis of negative shear lag in laminated composite cantilever beam. J. Aerosp. Eng. 33 (1), 04019103.

Song, Y., Min, J., Gao, W., 2019. Wearable and implantable electronics: Moving toward precision therapy. ACS Nano 13 (11), 12280–12286, PMID: 31725255.

Su, Y., Li, S., Li, R., Dagdeviren, C., 2015. Splitting of neutral mechanical plane of conformal, multilayer piezoelectric mechanical energy harvester. Appl. Phys. Lett. 107 (4), 041905.

Sunwoo, S.-H., Ha, K.-H., Lee, S., Lu, N., Kim, D.-H., 2021. Wearable and implantable soft bioelectronics: device designs and material strategies. Annu. Rev. Chem. Biomol. Eng. 12, 359–391.

Weerasinghe, A., Lu, C.-T., Maroudas, D., Ramasubramaniam, A., 2017. Multiscale shear-lag analysis of stiffness enhancement in polymer–graphene nanocomposites. ACS Appl. Mater. Interfaces 9 (27), 23092–23098.

Williams, D., 1951. Load distribution in riveted and spot-welded joints. Proc. Inst. Mech. Eng. 165 (1), 141–147.

Yang, J.C., Mun, J., Kwon, S.Y., Park, S., Bao, Z., Park, S., 2019. Electronic skin: Recent progress and future prospects for skin-attachable devices for health monitoring, robotics, and prosthetics. Adv. Mater. 31 (48), 1904765.

Zhao, Z., Liu, K., Liu, Y., Guo, Y., Liu, Y., 2022. Intrinsically flexible displays: key materials and devices. Natl. Sci. Rev. 9 (6), nwac090.